



Research papers

Characterizing and hindcasting ripple bedform dynamics: Field test of non-equilibrium models utilizing a fingerprint algorithm



Carter B. DuVal^{a,*}, Arthur C. Trembanis^a, Adam Skarke^b

^a University of Delaware, College of Earth, Ocean, and Environment, School of Marine Science and Policy, Newark, DE 19716, USA

^b Mississippi State University, Department of Geosciences, Mississippi State, MS 39762, USA

ARTICLE INFO

Article history:

Received 29 June 2015

Received in revised form

24 November 2015

Accepted 30 December 2015

Available online 14 January 2016

Keywords:

Ripple

Bedform

Morphodynamics

Fingerprint

ABSTRACT

Ripple bedform response to near bed forcing has been found to be asynchronous with rapidly changing hydrodynamic conditions. Recent models have attempted to account for this time variance through the introduction of a time offset between hydrodynamic forcing and seabed response with varying success. While focusing on temporal ripple evolution, spatial ripple variation has been partly neglected. With the fingerprint algorithm ripple bedform parameterization technique, spatial variation can be quickly and precisely characterized, and as such, this method is particularly useful for evaluation of ripple model spatio-temporal validity. Using time-series hydrodynamic data and synoptic acoustic imagery collected at an inner continental shelf site, this study compares an adapted time-varying ripple geometric model to observed field observations in light of the fingerprint algorithm results. Multiple equilibrium ripple predictors are tested within the time-varying model, with the algorithm results serving as the baseline geometric values. Results indicate that ripple bedforms, in the presence of rapidly changing high-energy conditions, reorganize at a slower rate than predicted by the models. Relict ripples were found to be near peak-forcing wavelengths after rapidly decaying storm events, and still present after months of sub-critical flow conditions.

© 2016 Elsevier Ltd. All rights reserved.

1. Introduction

Spatio-temporal variability in hydrodynamic forcing (e.g. wave, current or combined flow) complicate attempts to model ripple morphodynamics in the inner-continental shelf environment. Because the organization of ripples are mostly dependent upon dominant hydrodynamic conditions, sediment composition, or some combination of the two (e.g. [Wiberg and Harris \(1994\)](#)), spatial variability in forcing conditions would be expected to produce different configurations of ripple bedforms spacing (wavelength) and orientation, even within relatively small ripple fields. Consequently, attempts to model temporal evolution of ripple bedforms, which typically focus on one representative value (e.g. mean wavelength and orientation) have trouble predicting spatial distribution in ripple morphology, and multiple field and laboratory studies have shown that most semi-empirical ripple models do not accurately predict actual field measurements ([Li and Amos, 1998](#); [Camenen, 2009](#); [Pedocchi and García, 2009](#)). One limiting factor to empirical modeling has been accurately recording and measuring ripple spatio-temporal evolution ([Davies and](#)

[Thorne, 2008](#); [Skarke and Trembanis, 2011](#)).

In previous studies, ripple geometry was quantified from sea-floor imagery using various methodologies. Manual image interpretation is the most fundamental means of deriving ripple data from seafloor backscatter imagery (e.g. [Traykovski et al. \(1999\)](#)). The subjectivity of individual interpretations, however, leads to concerns over repeatability and variability between observers, aside from the impracticality of characterizing large fields of ripple bedforms ([Skarke and Trembanis, 2011](#)). Studies have thus turned to more automated methods, such as frequency-transform analysis (e.g. [Voulgaris and Morin \(2008\)](#) and [Maier and Hay \(2009\)](#)). This method converts acoustic imagery into the frequency domain through Fourier or other transforms, resulting in two-dimensional power spectrum in frequency space. Despite the improvement over manual analysis, there remain significant limitations to this method, including but not limited to the inability to disambiguate ripple orientation variability from wavelength variability ([Skarke and Trembanis, 2011](#)).

Instead, [Skarke and Trembanis \(2011\)](#) adapted a methodology for extracting ripple orientation and wavelength from side-scan imagery built around algorithms designed to extract biometric fingerprint statistics (see [Hong et al. \(1998\)](#) and [Felzenberg \(2009\)](#)). This method analyzes ripple imagery and assigns statistical values to each individual pixel, allowing the user to quantify

* Corresponding author.

E-mail address: cduval@udel.edu (C.B. DuVal).

ripple variability and distribution across a spatial domain. Rippled regions are assigned a reliability parameter, which is the ratio of backscatter intensity variability parallel and orthogonal to ripple crest orientations and represents the extent to which the bed is organized into a linear trough and crest morphology. This allows the user to set a minimum threshold to mask out areas that exhibit non-rippled as well as poorly organized or non-resolved ripple morphology. Orientation values are estimated using Gaussian filtered backscatter gradients to locate ripple crests, from which localized ripple wavelength values are derived (for further information on methods see Skarke and Trembanis (2011)). Additionally, the algorithm contains a method for isolating ripple defects by filtering and thinning backscatter images to isolate ripple crest lines. In all, the method presented by Skarke and Trembanis (2011) is better suited than previous approaches for the determination of the spatial variability of ripple morphology and is particularly useful for evaluation of ripple model validity (e.g. Goldstein et al. (2013) and Zare and Cobb (2013)).

Numerous empirical ripple models have been proposed over the last few decades (e.g. Nielsen (1981), Grant and Madsen (1982), Wiberg and Harris (1994), Traykovski et al. (1999) and Soulsby and Whitehouse (2005)) in attempts to better predict ripple dynamics. Instead of relating ripple height and wavelength to instantaneous surface wave conditions, multiple studies (Soulsby and Whitehouse, 2005; Doucette and O'Donoghue, 2006; Austin et al., 2007; Traykovski, 2007; Voulgaris and Morin, 2008, Soulsby et al., 2012) note that ripples exhibit a delayed response to changes in flow. Recent models have attempted to address these shortcomings. Traykovski (2007) adapted a non-equilibrium ripple model to allow for ripple reaction to lag behind hydrodynamic conditions. The lag is quantified using a variable timescale defined by the ripple cross-sectional area divided by the sediment transport rate (Traykovski, 2007). Subsequently, Soulsby et al. (2012) developed a time-dependent ripple calculation based upon the general derivative:

$$\frac{dx}{dt} = a(t) - b(t)x(t) \quad (1)$$

where x may represent ripple wavelength (λ), height (η), or orientation (ϕ). Equilibrium ripple predictors (e.g. Soulsby and Whitehouse (2005)) are used to calculate the values for x . The equation coefficients $a(t)$ and $b(t)$ are time varying values calculated by the expressions:

$$a(t) = \frac{\beta}{T_e} x_{eq} \quad (2)$$

$$b(t) = \frac{\beta}{T_e} + \frac{1}{T_b} \text{bio} \quad (3)$$

where the 'bio' variable is a switch for biodegradation to ripple height, controlled by biological half-life variable (T_b). The coefficient T_e is defined as the time scale for ripple evolution (such as wave period for wave dominant conditions), and β describes the rate change in ripple characteristics based on hydrodynamic conditions, derived from the wave mobility parameter (ψ) and critical threshold values. Further, the model incorporates wave or current dominated conditions, based on near bed shear stress values, to determine which ripple geometry prediction will be utilized in the calculation at time (t).

The results of the model were observed by Soulsby et al. (2012) to be promising, though there was the noted tendency of the model to underpredict ripples wavelengths in large-wave events (e.g. storms). They concluded by outlining a number of potential improvements to the model, including incorporation of other

“more accurate” predictors for large ripple wavelengths and heights. As such, the goal of this study is to extend the Soulsby et al. (2012) model, comparing the accuracy of three equilibrium ripple predictors within the model to field observations. With the fingerprint algorithm results serving as the baseline geometric values, the ability of the ripple model to predict temporal evolution can be tested with field observations. Further, we examine the performance of the non-equilibrium component in light of the fingerprint algorithm findings, and consider factors complicating ripple geometric predictions. Observations from this study highlight the variability of ripple morphodynamics on the inner-shelf.

2. Study site

Field observations were collected at the Redbird Artificial Reef (Fig. 1), an area encompassing 3.4 square kilometers of seafloor located approximately 30.5 km east of Indian River Inlet, Delaware (DNREC, 2009–2010). The reef is located within the Cape May shoal-retreat massif, created by the recent Holocene shoreline transgression of the Delaware River estuary system (Swift et al., 1980). The shoal and swale system trends NE–SW around the reef, with a prominent ridge northwest of the reef. Situated within a swale, the field site ranges from 21 to 29 m water depth. The central and southern areas of the reef are a mixture of fine, sometimes silty, clayey sand, and coarse gravelly sand likely deposited by the ancestral Delaware River or tributaries during the late Wisconsinan (Fletcher et al., 1992; Raineault et al., 2013). The reef is composed of various structures, including 997 New York City subway cars and 11 large vessels placed between 1996 and 2009 (DNREC, 2009a,b). Scour moats around the objects often expose coarse pre-Holocene sediment buried as shallow as 0.25 m from the surface (Raineault et al., 2013). In a study of the Redbird reef, Raineault et al. (2013) indicated that the seabed boundaries between the fine, silty sand and coarse gravelly sands were persistent, although they migrated slightly southwards over the course of multiple years. Also noted at the site were persistent sorted bedforms, possessing large wave orbital ripples. Large scour pits were also observed around the reef objects. These were often comet-shaped, extending to the west-southwest, which is the typical direction of forcing from large-wave events at the site (Raineault et al., 2013). The boundaries of the comet-shaped scour pits around the reef objects were noted to change annually.

As with much of the Mid-Atlantic bight, seabed morphodynamics at Redbird Reef are largely driven by waves from episodic storm events. Low to moderate tidal currents (~ 15 – 20 cm/s M2 tidal amplitude) are typical of average conditions in this region with peak bed stress and sediment transport during high energy events (Münchow et al., 1992; Wright, 1995). While experiencing both tropical and extra-tropical storm events, ‘nor’easters’ are the more frequent systems, usually occurring from late October to early March. The highest winds and waves from these events come out of the northeast and east-northeast, with waves often exceeding 4 m significant wave height and mean currents over 50 cm/s offshore (Wright, 1995). Events similar to the 1991 ‘Halloween Storm’ have generated waves over 6 m in height, mean currents near 50 cm/s and near-bed orbital velocities over 140 cm/s (Madsen et al., 1993; Wright et al., 1994). During Hurricane Sandy, which was observed during this study, significant wave height was greater than 7 m and orbital velocities reached 160 cm/s (Trembanis et al., 2013).

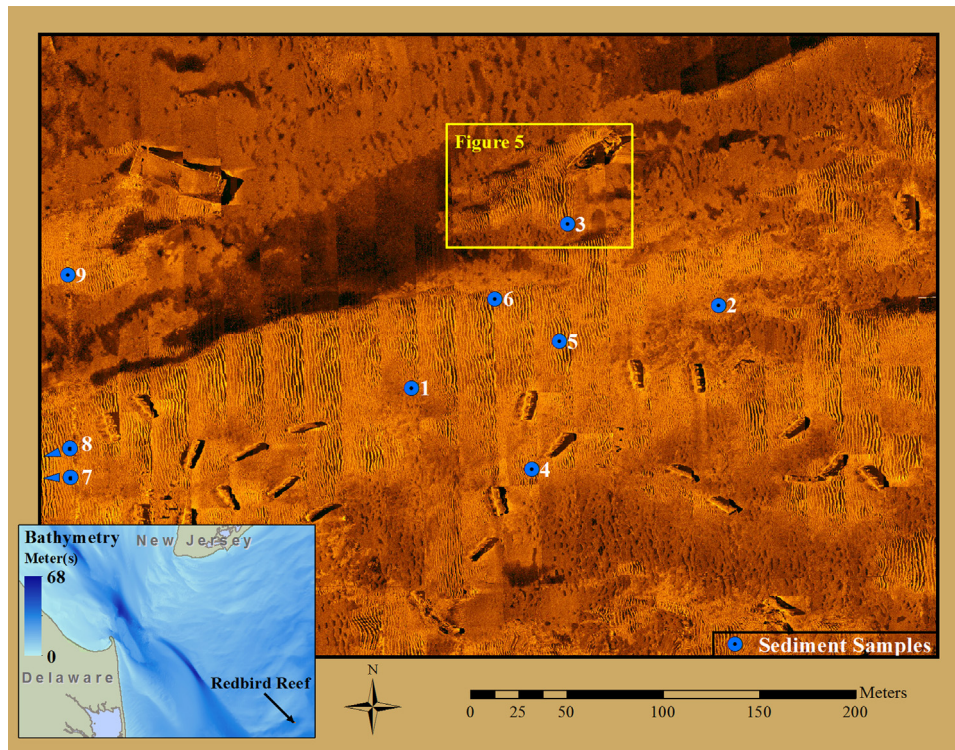


Fig. 1. Sonar backscatter of the study area within the Redbird Artificial Reef off of Delaware (inset). Sediment samples used for ripple predictions are marked in blue. Fingerprint algorithm example location (Fig. 5) is outlined. Instrument frame was located at sample 6 site. (For interpretation of the references to color in this figure legend, the reader is referred to the web version of this article.)

3. Methods

3.1. Instrumentation

Ripple bedform imagery was collected during four surveys (Oct. 26 and Nov. 10, 2012 and Mar. 29 and Jul. 29, 2013) conducted with a Teledyne Gavia Autonomous Underwater Vehicle (AUV). The vehicle is equipped with a Marine Sonics Technology dual-frequency side-scan sonar (900 kHz and 1800 kHz), and a Kongsberg GeoAcoustics GeoSwath phase-differencing bathymetric sonar (500 kHz). Repetitive 900 kHz side-scan and 500 kHz bathymetric surveys were conducted over a 0.25 km² subsection (see Fig. 1) of the reef, as well as multiple additional side-scan and camera surveys throughout the entire reef site.

Time series of hydrodynamic conditions were recorded using an *in situ* instrumented frame equipped with a 600 kHz upward facing Teledyne RDI Sentinel Workhorse Acoustic Doppler Current Profiler (ADCP) mounted 50 cm above the seabed collecting wave and current data, and a 2 MHz Nortek Aquadopp high-resolution Pulse-Coherent ADCP (PC-ADCP) to analyze near bed flow

Table 1

Acoustic sensor setting for deployments at Redbird Reef.

	PC-ADP	ADCP	Rotary
Frequency	2.1 MHz	600 kHz	2.25 MHz
Orientation	Downward	Upward	Horizontal
Time interval	30 min	30 min (current) 60 min (wave)	60 min
Samples	2400	100 (current) 1200 (waves)	2
Sample rate/Time	4 Hz	10 min	N/A
Bin size	0.3 m	1 m	N/A
Range/Depth	0.45 m	27 m	9 m 6 m
Height (off bottom)	0.4 m	0.5 m	1.05 m

(Table 1). The ADCP recorded conditions over a total of 158 days on four separate deployments (Aug.–Sept. and Oct.–Nov. 2012; Mar.–Jun. and Jul.–Sept. 2013), while the Aquadopp captured bottom conditions for 84 days on two deployments (Oct.–Nov. 2012; Mar.–Jun. 2013). Combined current vectors from the total ADCP record were processed for tidal harmonics and currents using the Matlab toolbox ‘t_tide’ (Pawlowicz et al., 2002). Near bed current predictions were extrapolated from t_tide based on analysis of the Aquadopp observations. Direct observations were augmented by wave data from NOAA buoy 44009, a method previously implemented for Redbird Reef by Raineault et al. (2013). The buoy is situated 23 km south of Redbird Reef, and is moored at a similar distance from the coast (30.5 km) and in similar water depth (30.5 m). The buoy has been operational since 1984, and offers a nearly complete historical record of wave height and period since that time. Comparisons between buoy 44009 and Redbird ADCP significant wave height (H_s) and peak period (T_p) show an $r^2=0.958$ and $r^2=0.801$ correlation respectively, with the buoy recording slightly higher wave heights on average (Fig. 2). During the research collection period, the buoy was offline between Dec. 03, 2012 and Feb. 22, 2013. NOAA WaveWatch3 (WW3) hind-casting was used to fill in this gap. The Wave Watch 3 data was found to underpredict wave heights for the Redbird Reef area, but was corrected using a linear transform. Comparison between the corrected WW3 and Redbird ADCP H_s show an $r^2=0.95$ correlation, although the T_p comparison yields a weaker correlation ($r^2=0.535$). For the purposes of this study, the WW3 corrected data is sufficient to complete the wave record for the given dates. Bottom orbital velocities were estimated using linear wave theory, specifically:

$$U_b = \frac{\pi H_s}{T_p \sinh(kh)} \quad (4)$$

where H_s is the significant wave height, T_p is the peak period, h is

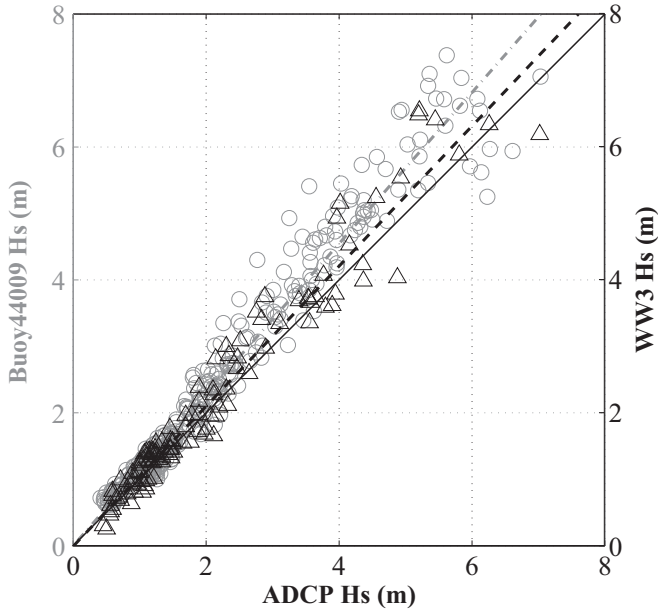


Fig. 2. Redbird ADCP significant wave height correlation to Buoy 44009 and Wave Watch 3 hindcasts.

the depth and wave number (k) is defined by:

$$k = \frac{2\pi}{L} \quad (5)$$

and L is the surface wavelength. When available, U_b was calculated from the Aquadopp ($2 \times$ rms of the horizontal velocity).

Bottom orbital velocity estimations derived from buoy 44009 wave conditions showed an $r^2=0.86$ correlation with those calculated from ADCP wave measurements.

3.2. Time-dependent ripple bedform calculation

The time-dependent derivative of Soulsby et al. (2012) was presented in the introduction. For the equilibrium ripple predictors, which are fed into the derivative, Soulsby et al. (2012) used equations from Soulsby and Whitehouse (2005). However, the nature of the model allows the user to choose which equilibrium ripple predictor to apply in the model, and in this regard we are not the first to do so. Soulsby et al. (2012) indicated that the time-varying model could be modified to take any wave-induced equilibrium ripple prediction, which was tested by Skarke (2013) using Wiberg and Harris (1994), Soulsby and Whitehouse (2005) and Traykovski (2007) ripple equations. Similarly, this study investigated the wave-induced equilibrium ripple predictions from Soulsby and Whitehouse (2005), Traykovski (2007) and Nelson et al. (2013). Current-generated ripple wavelength and height predictions are calculated using Soulsby et al. (2012) equations:

$$\eta_{max} = d_{50} 202 D_*^{-0.554} \quad (6)$$

$$\lambda_{max} = d_{50} (500 + 1881) D_*^{-1.5} \quad (7)$$

where D_* is the dimensionless grain diameter defined by equation 3.2 in Soulsby and Whitehouse (2005). The Soulsby et al. (2012) model includes conditions for current sheet-flow and washout also based on D_* values, which are integrated here. Wave orbital ripple wavelength predictions from Soulsby et al. (2012) are the empirically derived equations:

$$\frac{\lambda}{A} = \left[1 + 1.87 \cdot 10^{-3} \Delta \left(1 - \exp \left\{ - \left(2.0 \cdot 10^{-4} \Delta \right)^{1.5} \right\} \right) \right]^{-1} \quad (8)$$

where A is the wave orbital amplitude, and Δ is the wave orbital amplitude over median grain diameter. Here, we will also use the Traykovski (2007) wave orbital ripple predictors for coarse sands, defined by

$$\lambda_{eq} = 0.75 d_{0,1/3} = \frac{1.5 U_{b,1/3}}{\omega_r} \quad U_{b,1/3} \leq 4.2 w_s \quad (9)$$

$$\lambda_{eq} = \frac{1.5 (4.2 w_s)}{\omega_r} \quad U_{b,1/3} > 4.2 w_s \quad (10)$$

where d_0 is the wave orbital diameter and the subscript 1/3 represents the significant value (average of the highest one-third), U_b is the significant orbital velocity, w_s is the settling velocity and ω_r is the wave radian frequency. Lastly, we also used the Nelson et al. (2013) empirically derived equations for wave orbital ripples under regular and irregular waves, using numerous lab and field data sets. The collapsed function, a least squares fit between the irregular and regular wave predictions, is given by the equation,

$$\frac{\lambda}{A} = \left(\frac{0.72 + 2.0 \cdot 10^{-3} A}{d_{50} \left\{ 1 - \exp \left[- \left(\frac{1.57 \cdot 10^{-4} A}{d_{50}} \right)^{1.15} \right] \right\}} \right)^{-1} \quad (11)$$

Wave orbital ripple height values, which were not the focus of this study, are calculated in our models for purposes of incorporating bedform roughness to shear stress estimates using Nielsen (1981) ripple roughness. We chose to use the Nelson et al. (2013) empirically derived expression for ripple height under irregular waves:

$$\eta = 0.126 \lambda^{1.05} \quad (12)$$

excluding the calculations driven by Soulsby and Whitehouse (2005) equations, which use their inherent ripple height calculations. The Soulsby et al. (2012) biodegradation term, which models biological effects on ripple height alone (and not wavelength or orientation), is not included in this paper. As noted in their study, the term has not been tested against observations, and should be calibrated at study sites with sufficient biological information (Soulsby et al., 2012). Such observations were not collected in this study, and thus the term is withheld here.

We have incorporated conditional statements for anorbital ripple formation during strong orbital currents based on Wiberg and Harris (1994). Anorbital ripple formation occurs when the ratio of orbital diameter to anorbital ripple height exceeds 100, as calculated by the non-iterative expression (Malarkey and Davies, 2003) from Wiberg and Harris (1994):

$$\frac{d_0}{\eta} = \exp \left[C_1 - \sqrt{C_2 - C_3 \ln \left(\frac{d_0}{\lambda} \right)} \right] \quad (13)$$

where $C_1=7.59$, $C_2=33.60$, $C_3=10.53$ and λ is the anorbital wavelength or $535d$.

To determine when and under what dominant forcing regime bedforms are generated, threshold of sediment motion is calculated using the dimensionless Shields parameter, given by the expression:

$$\theta = \frac{\tau}{(\rho_s - \rho)gd} \quad (14)$$

where ρ_s is the density of sediment grains, g is the gravitational

acceleration and d is the sediment grain diameter. Under dominant unidirectional current forcing (U_c), τ is defined by the equation

$$\tau_c = \rho C_d U_c^2 \quad (15)$$

where C_d is the dimensionless coefficient of drag. This is calculated as:

$$C_d = \left(\frac{0.4}{1 + \ln\left(\frac{z_0}{h}\right)} \right) \quad (16)$$

where h is the water depth and z_0 is the elevation that $U_c=0$, which is related here to effective bed roughness (k_b). Under dominant oscillatory forcing (U_b), τ is expressed as:

$$\tau_w = \frac{1}{2} \rho f_w U_b^2 \quad (17)$$

where f_w is the wave friction factor, calculated using the Soulsby et al. (1993) empirically derived variant of the Swart (1974) formula. The Soulsby et al. (1993) equation is defined as:

$$f_w = 1.39 \left(\frac{A}{z_0} \right)^{-0.52} \quad (18)$$

where with rippled seabed, z_0 is determined by effective bed roughness (k_b). Sediment grain critical threshold is defined using the Soulsby and Whitehouse (1997) empirical Shields parameter:

$$\theta_{cr} = \frac{0.3}{1 + 1.2D_*} + 0.055[1 - \exp(-0.02D_*)] \quad (19)$$

where D_* is “dimensionless” grain size, defined as:

$$D_* = \left[\frac{g(s-1)}{\nu^2} \right]^{\frac{1}{3}} d \quad (20)$$

where ν is the kinematic viscosity of water and $s = \rho_s/\rho$. In this model, when critical shear stress is met, the dominant forcing regime is determined by the greater shear stress estimate (e.g. $\theta_c < \theta_w$), as suggested by Soulsby et al. (2012).

4. Results

4.1. Hydrodynamic conditions

Hydrodynamic conditions were compiled and calculated to approximate on site conditions from the combined buoy 44009 and Wave Watch 3 data from January 2012 through December 2013. Fig. 3 shows the significant wave height (H_s), peak period (T_p), estimated bottom orbital velocity (U_b), and estimated tidal near bed current (U_c). Annual averages are comparable to annual wave height, period and near-bed orbital velocity statistics calculated by Raineault et al. (2013) for the Redbird reef site from 2008 through 2011 (Table 2).

During the course of the study, three large storm events took place. Hurricane Sandy passed north of the reef on Oct. 28–29, 2012, generating significant wave heights over 7.1 m with periods of up to 14 s at the site. This was followed by a nor'easter 7 days later, which generated waves over 4.8 m with periods up to 14 s. The instrument mooring at the site, as well as Buoy 44009, captured both events. The third storm event took place March 6–8, 2013, which generated waves up to 7.8 m, again with periods up to 14 s, as captured by Buoy 44009. Residual surface currents during Hurricane Sandy and the trailing nor'easter indicate wind generated surface velocities with magnitudes up to 78 cm/s. Estimated bottom orbital velocities peaked at over 150 cm/s during hurricane Sandy, and nearly 120 cm/s in the following nor'easter.

Corresponding orbital velocity measurements derived from the bottom facing PC-ADCP showed orbital velocities measured 20 cm above the bed to be nearly 160 cm/s for both Sandy and the following nor'easter. Measured mean bottom currents during the storms peaked at 73 cm/s and 63 cm/s respectively. Estimated orbital velocities for the March 2013 nor'easter reach over 150 cm/s, with sustained orbital velocities between 50 and 100 cm/s lasting for 72 h after the storm. Shields parameter (θ) sediment threshold and shear stress values estimated from grain size analysis of *in situ* grab samples indicate high levels of fine grain sediment suspension and transport during both storms, with sustained fine-medium sediment movement following Sandy, but quickly dropped below threshold values following the nor'easter (Fig. 4).

4.2. Fingerprint algorithm

Detectable ripple bedforms were found only in the latter three surveys, with the Oct. 26, 2012 survey showing a largely expressionless seabed. In stark contrast, the post storms survey of Nov. 10, 2012 showed extensive fields of ‘megaripples’ (wavelengths > 1 m), with orbital ripples also found within the scour patches behind the reef objects (Fig. 5). Spatial distribution maps derived from the fingerprint algorithm show ripple orientation (normal to the ripple crest) varied as much as 40 degrees, although the orientation distribution plot (Fig. 6a) shows a nearly normal distribution of ripple orientation, centered over a median orientation of 83.2 degrees (standard deviation 6 degrees). Ripple wavelength values vary spatially as well (standard deviation 0.36 m), with large, ‘megaripples’ found throughout the large sorted bedform field. Ripple wavelengths (Fig. 6b) ranged from around 0.25 to 2.4 m, with a median wavelength value of 0.975 m. The wavelength distribution is skewed towards smaller wavelengths (skewness 0.6).

The data from March 29, 2013 revealed further sorted bedform and scour field growth. The AUV survey occurred approximately 21 days following a strong Spring nor'easter that generated waves higher than Hurricane Sandy (> 7.8 m), though with near bed orbital velocities of similar magnitude (~150 cm/s). Within the three weeks following the storm, the ripple bedforms were observed to have already undergone decay and burial. Ripple orientation (Fig. 6a) shows a smaller standard deviation (5.3 degrees) than November, centered on a median orientation of 87.5 degrees. Ripple wavelength (Fig. 6b) still ranged from around 0.25 to 2.25 m, but with a much lower median (0.63 m) and trending (skewness 2.95) to smaller wavelength values. By the July 29, 2013, the fingerprint algorithm detected very few ripple bedforms in the study area. The majority of the orbital ripples in the sorted bedform and scour fields had undergone decay or burial in the extended period of low to moderate wave conditions following the March 2013 nor'easter. In July, ripple orientation (Fig. 6a) centered around 91.6 degrees, but with a higher standard deviation (6.6 degrees). Likewise, wavelength (Fig. 6b) varied more (0.52 m standard deviation), despite a similar range (0.25–2.25 m). The median wavelength in July was much higher than the previous datasets, at 1.15 m.

4.3. Non-equilibrium model prediction

Three versions of the non-equilibrium model using either Soulsby and Whitehouse (2005), Traykovski (2007), and Nelson et al. (2013) equilibrium predictors were compared using the Nov. 2012 ADCP data to determine the best ripple predictor for this environment. Each model ran nine separate grain sizes estimates determined from grab samples taken at known ripple locations before and after the storms. While it is typical to use d_{50} (median)

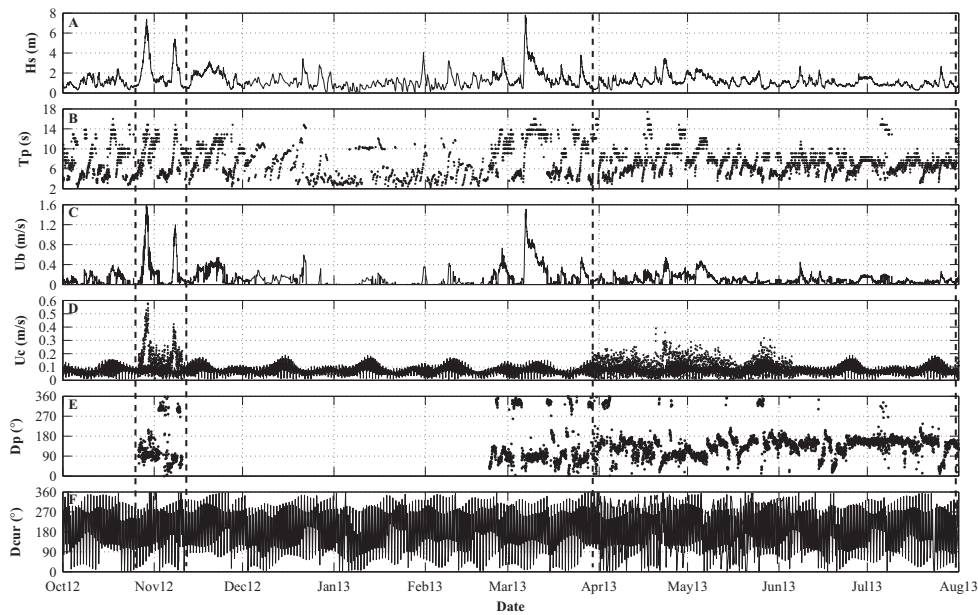


Fig. 3. Hydrodynamic conditions from Oct 2012 to Aug 2013. (A) Significant wave height. (B) Peak wave period. (C) Near-bed significant orbital velocity. (D) Near-bed tidal current predictions with direct measurements overlaid. (E) Buoy 44009 wave direction (unavailable for prior to Feb 22, 2013) augmented by direct measurements. (F) Current direction predictions augmented by direct measurements. Vertical dashed lines indicate the survey periods.

Table 2

Annual significant wave height, wave period, near-bed orbital velocity and predicted tidal currents at Redbird Reef. Hydrodynamic data from 2008–2011 from Raineault et al. (2013).

Year	H_s (m)	T_p (s)	U_b (cm/s)	U_c (cm/s)
2008	1.31	7.61	14.3	N/A
2009	1.33	7.48	14.4	N/A
2010	1.22	7.66	13.4	N/A
2011	1.13	7.34	12	N/A
2012	1.14	7.29	9.91	7.77
2013	1.15	7.31	10.1	7.78

grain sizes for ripple model predictions, sediment grain size distribution data was used to generate a weighted mean grain size for each sample in an attempt to better represent the actual sample grain size distributions (Table 3). Weighted mean grain sizes were calculated by assigning the percentage contribution of a given grain size within the sediment sample distribution to the overall total sediment sample volume. Comparison to ripple observations indicated that both the models using Soulsby and Whitehouse (2005) and Nelson et al. (2013) equations largely underpredicted ripple wavelength at the site (Fig. 7). This finding corroborates a noted issue with the Soulsby and Whitehouse (2005) equation in

large-wave events (Soulsby et al., 2012). Similarly, it has previously been observed that the Nelson et al. (2013) equations tended to underpredict wavelength in very coarse sediments (personal comm. George Voulgaris, Nov. 7, 2014). The model using Traykovski (2007) wavelength predictions were considerably higher than the other two models. Comparing the model distribution to the fingerprint algorithm distribution (Fig. 8), the model predicted the largest ripple wavelength at 1.55 m, with only 12 percent of the observed wavelength distribution falling above that prediction. Likewise, the minimum wavelength prediction (0.6 m) excluded only 8 percent of the observed wavelength distribution. With the incorporation of conditions for coarse sediment in Traykovski's (2007) model, the closer fit of this model under the given environment is understandable. Given this model encapsulates 80% of the wavelength distribution measured by the fingerprint algorithm, Traykovski (2007) equilibrium predictor is used in the remaining non-equilibrium wavelength model results presented in this paper.

The adapted non-equilibrium ripple model estimates a high level of bedform activation and reorganization during Hurricane Sandy and the trailing nor'easter, conforming to earlier sediment threshold estimates. Based on the *in situ* ADCP measurements, the directional component of the model estimates a focusing of ripple orientation during the most intense periods of the storms: for Hurricane Sandy, ripple orientation (orthogonal to the ripple crest)

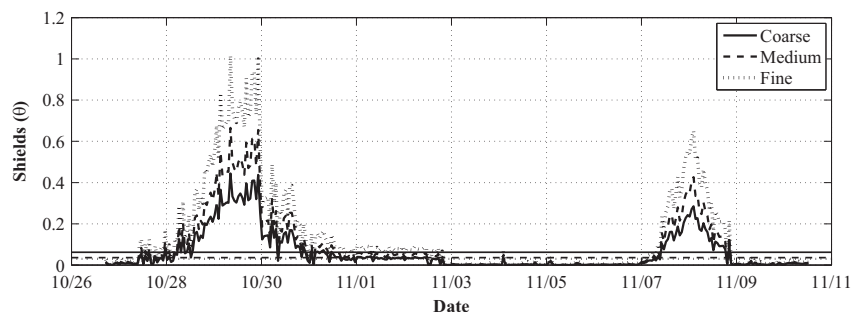


Fig. 4. Wave Shields critical threshold and observed Wave Shields values for three representative samples (0.17, 0.4 and 1 mm d_{50}) from Redbird Reef during Hurricane Sandy.

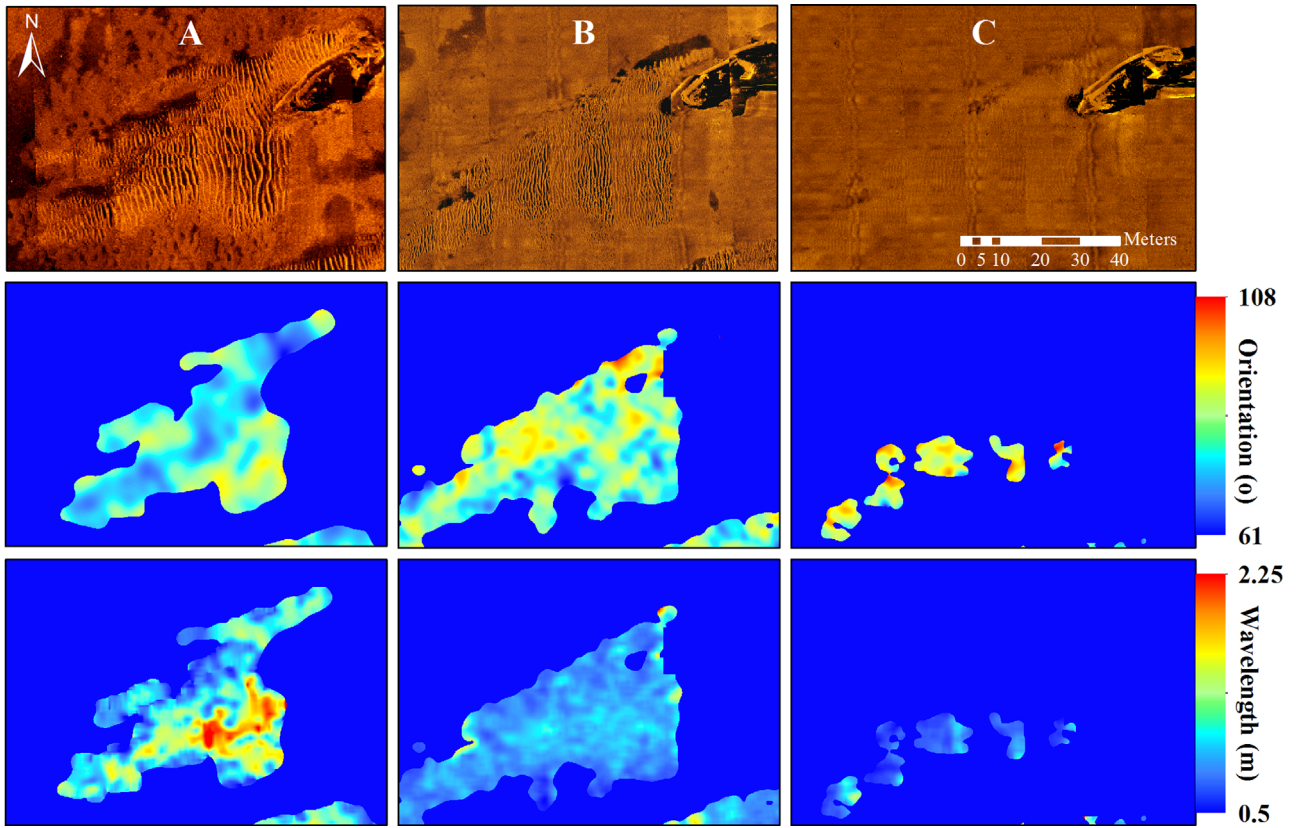


Fig. 5. Subsample of fingerprint algorithm orientation and wavelength results from (A) Nov. 11, 2012, (B) March 29, 2013, and (C) July 29, 2013.

focused near 113 degrees (standard deviation=0.28 degrees) and 80 degrees (standard deviation=0.55 degrees) during the nor'easter (Fig. 9a). These estimates reflect the dominant historical storm wave approach for tropical and nor'easter storms, respectively. As the storm conditions abated, the ripple orientation estimates deviated as conditions dropped below threshold limits for coarser samples, while finer sediment remained in movement. The highest wavelength values were predicted during the peaks of the storms for the coarser sediments. Samples with a weighted mean below 0.6 mm during Sandy and 0.47 mm during the nor'easter

slipped into anorbital ripple conditions (Fig. 9b). Despite largely different significant wave heights between storms, the model predicted nearly identical maximum ripple wavelength values for both Sandy and the nor'easter. U_b calculations from the *in situ* Aquadopp showed comparable near-bed orbital velocities during Sandy (> 150 cm/s) as with the nor'easter (> 140 cm/s), although not as sustained in the latter as in the former. The predicted ripple wavelengths do not decay at the end of the ADCP record as predicted after Sandy, but rather maintain values near the peak wavelength estimates during the nor'easter.

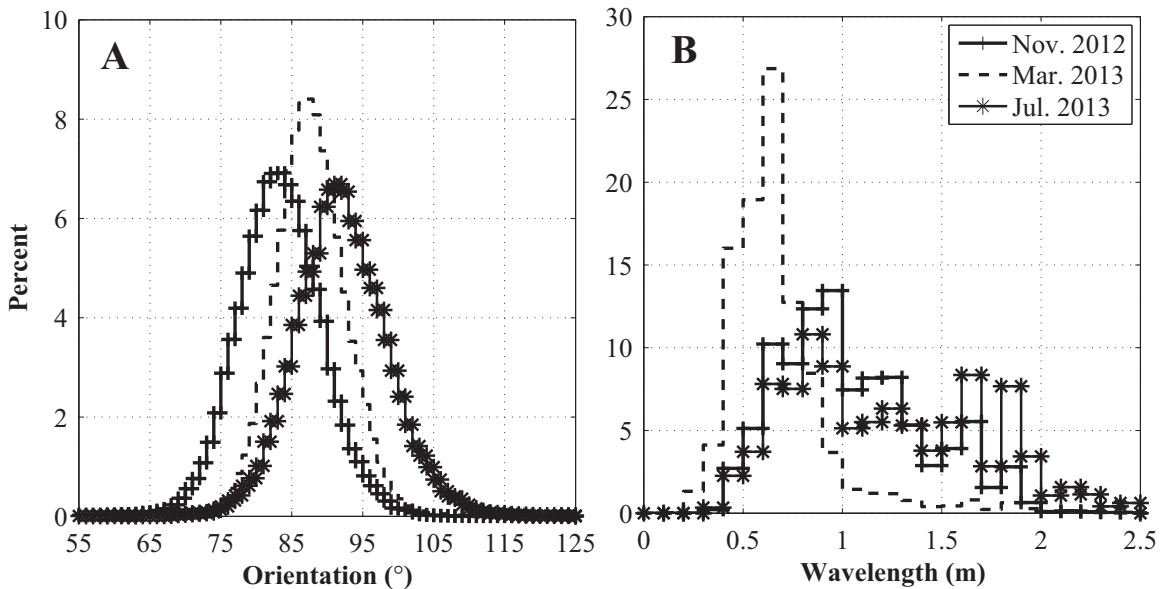


Fig. 6. Ripple orientation (A) and wavelength (B) distributions at Nov. 10, 2012, March 29, 2013, and July 29, 2013.

Table 3
Redbird grab sample weighted mean sediment sizes and Wentworth (1922) classification descriptor.

Sample number	1	2	3	4	5	6	7	8	9
Grain size (mm)	0.33	0.425	0.45	0.452	0.472	0.483	0.679	0.927	0.952
Description	Med	Med	Med	Med	Med	Med	Coarse	Coarse	Coarse

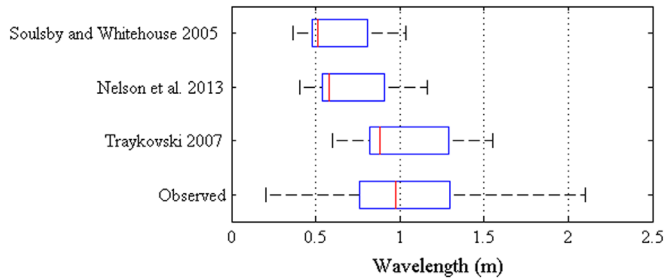


Fig. 7. Comparison of ripple wavelength models versus observed ripple wavelength distribution from Nov. 10, 2012. Outlying values are not shown here (minimum and maximum 1% of distribution).

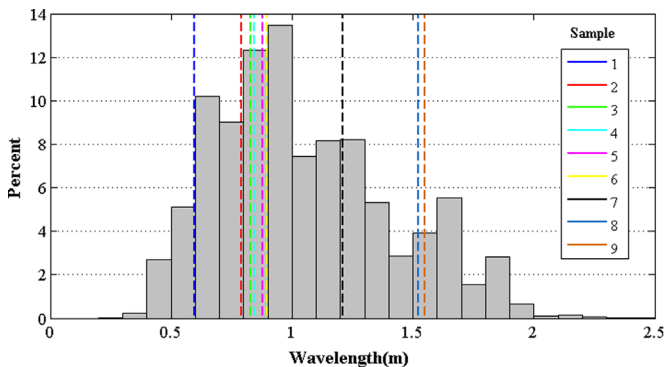


Fig. 8. Model results using Traykovski (2007) wavelength predictions compared to Nov. 10, 2012 observed ripple wavelength distribution.

The non-equilibrium model was applied using the combined NOAA buoy 44009 and Wave Watch 3 record (referred to from here as the buoy non-equilibrium model). Near bed wave-orbital velocity was estimated using linear wave theory (outlined above). Direct current observations were not available, so instead near bed tidal current estimates were used based on tidal harmonic analysis of *in situ* ADCP data from previous (Oct–Nov 2012) and subsequent deployments (March–June and July–Sept, 2013). The buoy non-equilibrium model results (Fig. 10) were compared to the March

29, and July 29, 2013 surveys to which no *in situ* hydrodynamic record was available. The model estimates a ripple reactivation between the March nor'easter and the March 29 survey, with peak ripple wavelength topping out around 1 m. Fingerprint algorithm statistics show that only 8 percent of observed ripple wavelengths fell above 1 m. However, the buoy non-equilibrium model indicates ripple wavelength decay for the coarsest sample at the time of the geoaoustic survey to only 0.62 m, for which over 52 percent of the observed wavelength distribution was greater (Fig. 10). Likewise, the largest predicted wavelength value at the time of the July survey was only 0.42 m, having dropped off from over 0.5 m only days before due to conditions just above critical threshold (Fig. 11). This estimate is lower than 99 percent of the ripple wavelength distribution observed at the site.

5. Discussion

5.1. Fingerprint algorithm

The fingerprint algorithm results indicate large spatial variability in ripple orientation and wavelength across the study area. Others have noted such variability in ripple orientation and wavelength within sorted bedform fields, albeit in sites with varying water depths and distance from shore (e.g. Cacchione et al. (1984) and Trembanis and Hume (2011)). While the Redbird reef site has little overall bathymetric relief, variability in the study area may have more to do with sediment composition, which differs considerably throughout the site. Another factor to consider is the effect of the reef objects on near-bed flow, and in turn adjacent ripple formation: the exposure of coarse sediment basements in the object scour pits, as noted by Raineault et al. (2013), allowed for localized ripple formation outside of the broader sorted bedform ripple field. Nevertheless, a fairly consistent juxtaposition occurred between the coarse, ripple-forming sediment and fine sediment at the site. Although small orbital or anorbital ripples have been observed to form in the finer sediments next to sorted bedforms (Murray and Thielert, 2004; Green et al., 2004), side-scan resolution limitations may have precluded detection by the

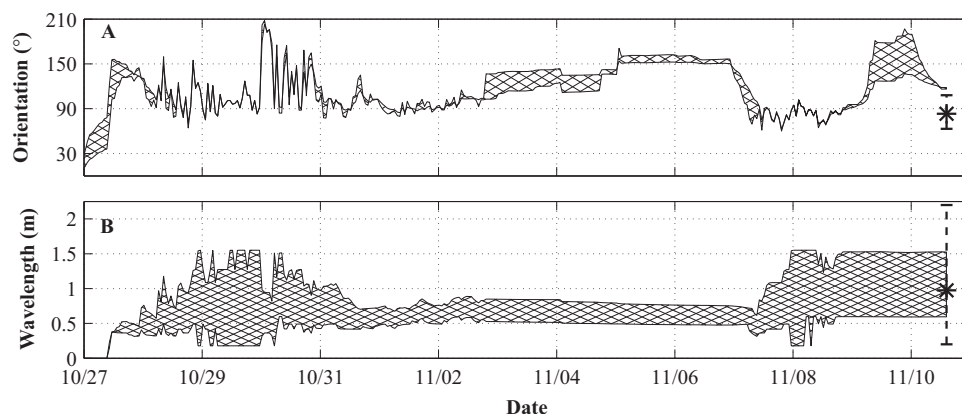


Fig. 9. Non-equilibrium orientation (A) and wavelength (B) predictions from Oct. 26 to Nov. 10, 2012 showing the impacts of Hurricane Sandy and the nor'easter on ripple orientation and wavelength distribution. Crosshatched area shows the model spread between finest and coarsest grain size. The dashed lines represent observed ranges at the time of the survey with asterisks marking the median value.

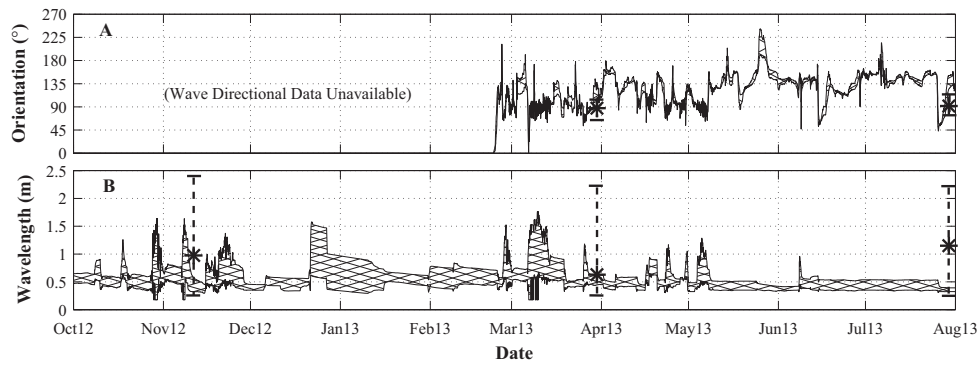


Fig. 10. Non-equilibrium orientation (A) and wavelength (B) predictions from Buoy 44009 data. Crosshatched area shows the model spread between finest and coarsest grain size. The dashed lines represent observed ranges at the time of the surveys with asterisks marking the median value. Note that wave direction data (D_p) was not available until Feb. 22, 2013.

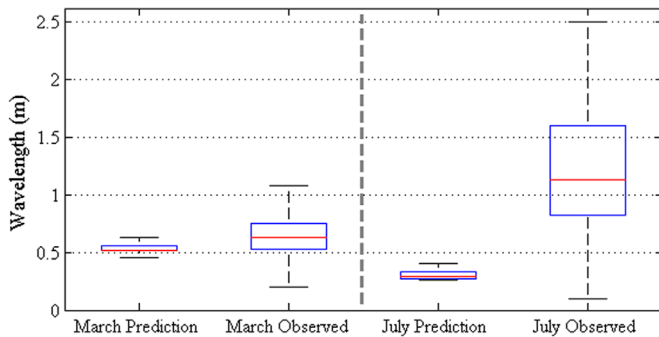


Fig. 11. Comparison of ripple wavelengths by adapted non-equilibrium ripple model using Traykovski (2007) wavelength predictions versus observed ripple distributions from March 29, 2013 to July 29, 2013. Outlying values are not shown here (minimum and maximum 1% of distribution).

fingerprint algorithm in this study given the algorithm's reliability threshold.

Peak ripple orientation from the Nov. 10, 2012 survey aligns more with dominant wave direction of the nor'easter, rather than Hurricane Sandy. Given the intensity of the nor'easter, ripple bedforms observed after the storm had reorganized to the dominant wave forcing conditions (e.g. direction and magnitude) during this nor'easter. Although the seabed signature is more indicative of the nor'easter's "fingerprint," the majority of scour and sediment transport likely occurred during Hurricane Sandy: the duration of high-energy conditions, in which all representative sediment types were in suspension at the site (Fig. 4), during Hurricane Sandy (~ 72 h) was almost twice that of the following nor'easter (~ 40 h).

The dominant wave direction from the March 2013 nor'easter correlates well with observed ripple orientation, with storm waves predominately from the east ($\sim 80^\circ$ to 100°). Despite conditions similar to Hurricane Sandy, the ripple wavelengths from the March 29, 2013 survey were significantly smaller than those found in the November survey. Comparisons of the storm near-bed orbital velocities indicate that the March nor'easter conditions decreased over a longer period of time (~ 72 h) than the rapidly decaying conditions from the November nor'easter. An associated reorganization of ripple wavelengths to decaying conditions would explain smaller wavelengths than expected, although the non-equilibrium model results suggest the bedforms reorganized to a smaller event following the nor'easter.

5.2. Non-equilibrium predictor

Discrepancies between the non-equilibrium model estimates and the March and July 2013 observed ripple wavelength suggest

an issue with either the Buoy or ADCP dataset. Reanalysis of the Nov. 2012 predictions using the Buoy 44009 conditions do not show the sustained ripple wavelengths indicated by the ADCP data, but rather a steep decrease in wavelength similarly estimated by the model after the March, 2013 nor'easter. Comparison between the buoy and ADCP model estimates during the Oct. and Nov. 2012 storms show fairly strong agreement ($r^2=0.76$) between the two model inputs up until the point of departure following the November nor'easter. Estimates derived from Buoy 44009 data indicate a period following the storm of reorganization until settling into much smaller wavelengths than observed (Fig. 12). Suspended sediment estimates derived from ADCP data indicate conditions rapidly fell below threshold of motion for the modeled sediment distribution, suggesting such reorganization would not have occurred. Slightly higher wave orbital velocities estimated from the buoy data following the storm result in the models' departures. The reorganization to larger ripple wavelengths in the ADCP model occur not once, but twice during the nor'easter, the latter of which occurred after peak storm conditions. To consider that peak storm wavelengths occurred during decaying storm conditions is suspect; the model event is triggered by a sharp, momentary increase in wave-orbital velocity in the trailing edge of the storm conditions. Examination of the ADCP data suggests that this is an artifact caused by an errant wave period measurement during one sampling event. The non-equilibrium model was rerun using wave orbital estimates derived from near-bed Aquadopp measurements to test this hypothesis. Results corresponded to the buoy 44009 results, suggesting continued ripple reorganization as the storm energy decreased. Thus, while the ADCP driven model shows sustained peak wavelengths after the nor'easter, these relict wavelength estimates are artifacts caused by an errant wave period measurement.

With this consideration, the ADCP relict wavelength estimates still most strongly compare to the observed ripple wavelength distribution in the Nov. 10, 2012 data, i.e., ripple wavelength observations are nearly identical to the estimated ripple wavelengths during the peak conditions of the nor'easter. This suggests that peak storm wavelength predictions correspond to the observed distribution from the Nov. 10, 2012 survey, and not the predictions concurrent to the geoaoustic survey after the storm. Moreover, ripple orientation observations correspond to model orientation predictions during the height of the storm, and again not to those predicted after the storm.

Similar agreement is found when comparing the March 2013 wavelength predictions to previous ripple reorganization events. Although wavelength predictions from a small event ($U_b \sim 50$ cm/s) that took place just 3 days prior to the March 29, 2013 survey would account for the skewed-smaller observed wavelength

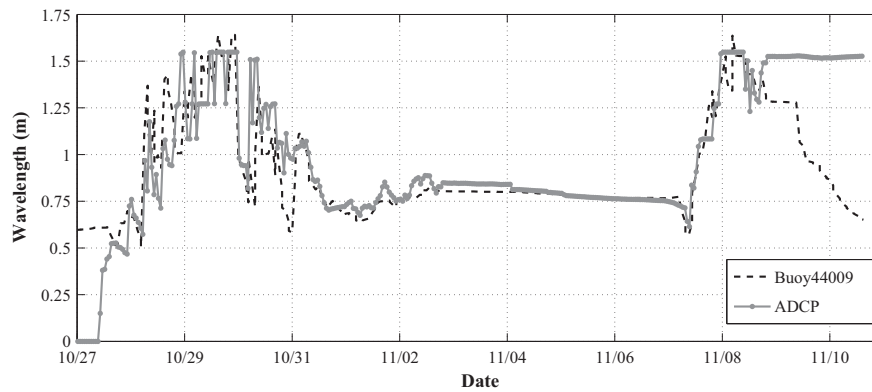


Fig. 12. Comparison of Buoy 44009 versus Redbird ADCP ripple wavelength predictions during the Oct–Nov. 2012 storms.

distribution, the observed ripples from the March 29, 2013 survey were already in a pronounced state of erosion and burial. It is unlikely for this erosion to have occurred in the short span between the March 26 predicted reorganization event and the survey, as the time span was nearly identical to that between the November nor'easter and Nov. 10, 2012 survey, where no significant erosion or burial was observed. With the tendency of the buoy-derived estimates to overpredict near-bed forcing, the observed ripples were more likely relict ripples from the extended waning period of the March nor'easter, and not recently reorganized ripples. The fact that other studies (e.g. Marsh et al. (1999), Traykovski et al. (1999) and Austin et al. (2007)) have observed relict ripples taking significant periods of time to respond to changing hydrodynamic conditions suggests this short event was not a major factor in ripple formation, albeit possibly a contributor to the observed ripple erosion (Traykovski et al. (1999) observed larger relict ripple eroding under small wave orbital currents). Furthermore, no predicted ripple reorganization event subsequent to the March nor'easter was strong enough to generate ripple wavelengths above 1.1 m, yet 54 percent of the ripple wavelength distribution recorded in July 29, 2013 fell above 1.1 m in wavelength. Given that the detectable ripple area for the July 29, 2013 survey was only 15 percent of the ripple area of March 29, 2013, larger relict ripples from the March 2013 nor'easter likely skew the observed ripple wavelength distribution from July. Ripple burial is commonly noted with sorted bedforms over periods of low-energy hydrodynamic conditions (Murray and Thieler, 2004; Green et al., 2004; Coco et al., 2007; Trembanis et al., 2007). Prior to the July survey, there was an extended period of low to moderate conditions during which many of the smaller ripple bedforms were possibly buried by fine sediments or subject to erosion. Only larger relict ripples would remain to be observed, skewing the distribution as seen here. Indeed, a subsection comparison between the fingerprint algorithm wavelength measurements from the March and July 2013 shows strong agreement ($r^2=0.81$), where only the smaller ripples are obscured between the surveys (Fig. 13). There is a slight increase in the wavelength of the remaining relict ripples is apparent despite no evident reworking. Voulgaris and Morin (2008) noted a similar pattern with relict ripples when using spectral wavelength analysis on time series imagery of ripple morphodynamics, and upon investigation of this pattern in the imagery, attributed this to natural diffusion processes of the ripples.

It is evident that near-peak storm ripple wavelengths are persisting under periods of waning forcing, despite conditions remaining above critical threshold for some time. The latency in ripple equilibration to the changing conditions appears to increase beyond the time between peak-energy forcing and decay to sub-

critical conditions. This decoupling of ripple response to forcing has been noted before. In developing his time-dependent model, Traykovski (2007) noted relict ripple wavelengths were near the maximums generated by large forcing events such as storms, and did not scale to decaying storm conditions. Austin et al. (2007), observing small wave-orbital ripples on a tidal beach, found asymmetrical responses in wavelength during flooding and ebbing tides despite nearly symmetrical patterns in hydrodynamic forcing during flood and ebb. While wavelength increased with rising tide, during falling tide, changes in wavelength lagged behind changes in hydrodynamic forcing, when reorganization to smaller ripple wavelengths was expected. Given these observations, Austin et al. (2007) concluded that the ripples formed during increasing forcing had become too large to be altered by the waning energy during falling tide, and that the rate of change in hydrodynamic forcing under tidal influence was far more rapid than the relaxation time of the large ripples. This supports the point above that, once established, ripples may take a significant amount of time to respond to changing forcing (e.g. Traykovski et al. (1999)).

The inability of the adapted non-equilibrium model to predict the observed relict ripples in this study may be explained in light of the site characteristics. The mean depth at Redbird Reef (28 m) is far deeper than typical ripple bedform studies. In the 49 studies listed and used by Nelson et al. (2013) to develop their empirical model, only three met or exceeded 28 m depths, with the majority in less than 10 m of water. The Soulsby et al. (2012) model was developed empirically and tested against flume and field sites of less than 7 m depth. Traykovski (2007) model used data from sites at 11 m and 14 m. In the case of the latter two studies, the magnitude of larger wave forcing events never topped an order greater than background conditions, and in the case of Soulsby et al. (2012), mean current conditions often met or exceeded near-bed orbital velocities, resulting in shifts between wave or current-dominated conditions and constant reworking of bedforms.

At Redbird Reef, due to the depth and location on the inner shelf, background conditions (as shown in Fig. 3) are characterized by, in comparison to the other studies, weak tidally driven currents with long periods of little-to-no wave orbital current at depth. Sediment transport and bedform morphodynamics are dominated by episodic large wave events with near bed wave-orbital velocities exceeding 100 cm/s, and often an order of magnitude higher than background conditions. At no times in the adapted model did current forcing exceed wave-orbital forcing when conditions exceeded critical thresholds. Considering these characteristics in light of the Austin et al. (2007) findings, it is likely that, despite constant super-critical forcing between waxing and waning storm conditions, the waning forcing conditions decay at a rate that far exceeds the relaxation time of the established

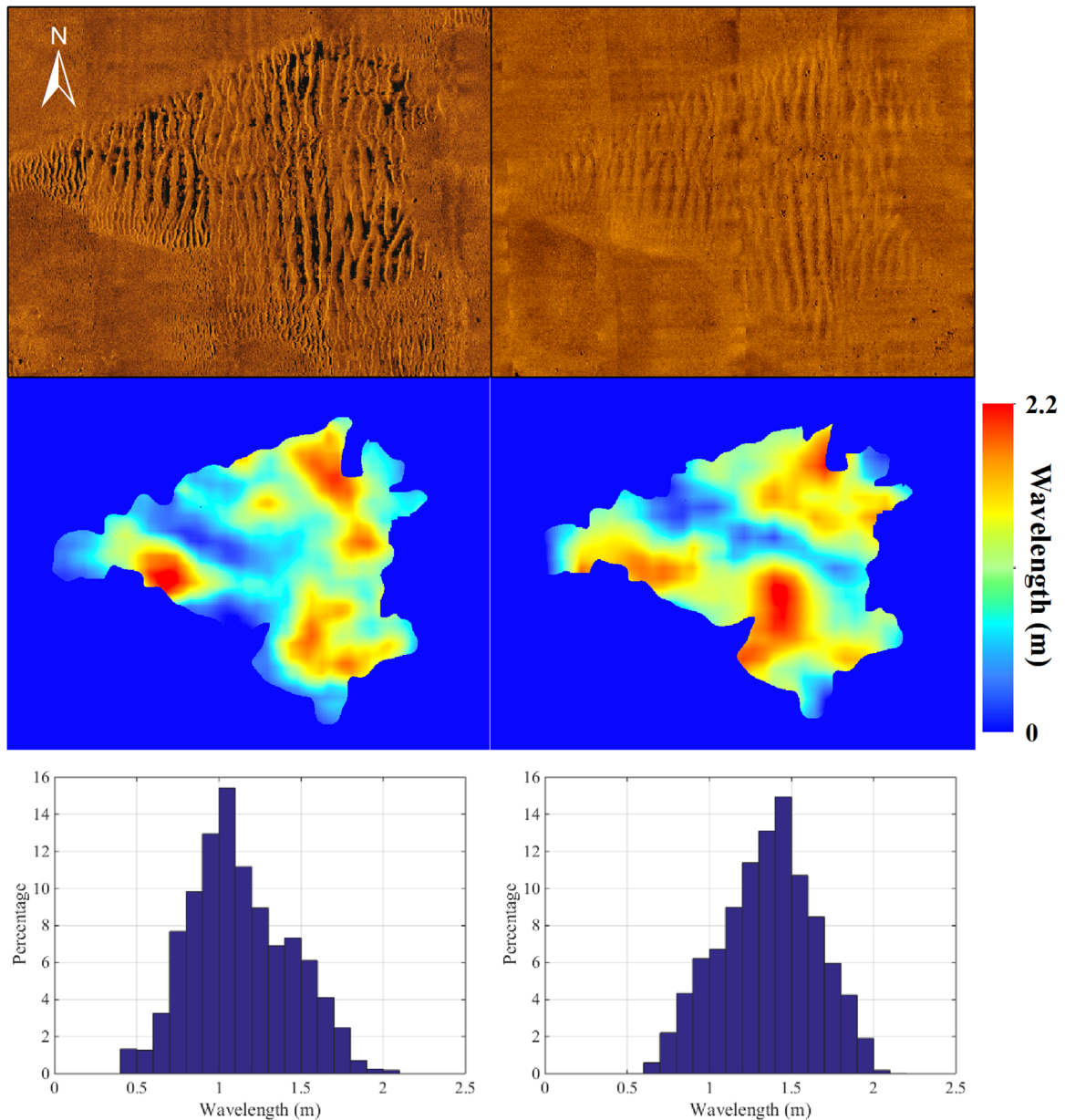


Fig. 13. A sample of (a) March 29, 2013 and (b) July 29, 2013 ripple bedforms. While degraded, the ripple bedforms imaged in July appear to be relict ripples from the March nor'easter. Ripple wavelength distributions are shown below.

'mega-ripples' at Redbird. With extended periods of low-to-moderate energy conditions, relict ripples remain at near-peak forcing wavelengths for weeks to months after formation, with smaller ripples buried or eroded by natural processes associated with sorted bedforms.

6. Conclusions

The fingerprint algorithm technique allows for in-depth study of ripple spatial variability across heterogeneous seabeds with high degrees of precision and reliability. Results from the fingerprint algorithm in this study demonstrate the need for predictive models to consider a distribution of ripple geometries rather than application of a single median representative value, especially in skewed populations. Additionally, the algorithm provides a baseline by which to compare and adapt ripple bedform models, and

when applied to temporal ripple imagery (e.g. rotary sonar), the ability to characterize non-equilibrium ripple evolution.

The comparisons in this study between the observed bedform wavelengths and an adapted non-equilibrium ripple model from Soulsby et al. (2012) and Traykovski (2007) indicate that ripple reorganization did not occur at the rate estimated by the adapted non-equilibrium model. Rather, it suggests that rapid decreases in near-bed forcing result in near-peak wavelength relict ripples. Several studies (e.g. Traykovski (2007) and Austin et al. (2007)) have come to similar conclusions. The extended presence of these relict ripples would undoubtedly have an impact on further ripple formation and evolution, affecting near bed turbulence (Hay, 2008) and new ripple formation patterns (Nelson and Voulgaris, 2014).

Consideration should be given to the depth of the study site that this adapted model was applied; instead of constant alteration between wave and current forcing found in shallower coastal

regions, this site, due to its depth and location, undergoes episodic high-energy forcing followed by extended periods of sub-critical conditions. This environment is favorable for the extended expression of relict ripples, rather than constant bedform evolution. However, the model incorporated a linear time dependency, which may not fully replicate time difference in forcing and bedform response. Rather, scaling time-dependency to sediment transport rates may be more appropriate, as suggested by previous studies in flumes (e.g. Smith and Sleath (2005)), and the field (e.g. Traykovski (2007)) and scour modeling (e.g. Whitehouse (1998) and Trembanis et al. (2007)), which results in exponentially decaying lag time between increased forcing and ripple evolution. Further attention should be given to effects of combined wave and current forcing on ripple geometry. While this model defaulted to the dominant forcing regime at a given time, the combined effect of wave and current forcing may account for deviations in ripple orientation (Amos and Collins, 1978; Li and Amos, 1998; Andersen and Faraci, 2003; Smyth and Li, 2005; Lacy et al., 2007) and wavelength that the model did not capture in this study.

Acknowledgments

The authors would like to acknowledge the Office of Naval Research for its support in this study (Bedform Parameterization and Object Detection From Sonar Data – Application of Fingerprint Algorithms Award number: N000141210303, ONR Bedforms Grad student support – Award number: N00014-14-1-0091). We would also like to thank Val Schmidt for his work with the AUV, Doug Miller for his support with benthic sampling, Trevor Metz and Justin Walker for their assistance in the field, and the captain and crew of the R/V Hugh R. Sharp for field operations. Thanks are due to Nicole Raineault, whose study in part laid the groundwork for future work at the Redbird Reef, and Bruce Lipphardt for his assistance with tidal analysis.

References

- DNREC, 2009a. 39 More Subway Cars Sunk at Delaware's Redbird Artificial Reef. News from the Delaware Department of Natural Resources and Environmental Control, vol. 39(250), June 02, 2009.
- DNREC, 2009b. 24 More Subway Cars Sunk to Enhance Habitat at Redbird Reef. News from the Delaware Department of Natural Resources and Environmental Control, vol. 39(269), June 16, 2009.
- Amos, C.L., Collins, M.B., 1978. Combined effects of wave motion and tidal currents on morphology of inter-tidal ripple marks – Wash, UK. *J. Sediment. Petrol.* 48, 849–856.
- Andersen, K.H., Faraci, C., 2003. The wave plus current flow over vortex ripples at an arbitrary angle. *Coast. Eng.* 47, 431–441.
- Austin, M.J., Masselink, G., O'Hare, T.J., Russell, P.E., 2007. Relaxation time effects of wave ripples on tidal beaches. *Geophys. Res. Lett.* 34, L16606.
- Cacchione, D.A., Drake, D.E., Tate, G.B., 1984. Rippled scour depressions on the inner continental shelf off central California. *J. Sediment. Petrol.* 55, 1280–1291.
- Camenen, Benoît, 2009. Estimation of the wave-related ripple characteristics and induced bed shear stress. *Estuarine Coast. Shelf Sci.* 84, 553–564.
- Coco, G., Murray, A.B., Green, M.O., 2007. Sorted bed forms as self-organized patterns: 1. Model development. *J. Geophys. Res. Earth Surf.* 112, F03015.
- Davies, A.G., Thorne, P.D., 2008. Advances in the study of moving sediments and evolving seabeds. *Surv. Geophys.* 29, 1–36.
- Doucette, J.S., O'Donoghue, T., 2006. Response of sand ripples to change in oscillatory flow. *Sedimentology* 53, 581–596.
- Felzenberg, J.A., 2009. Detecting Bedform Migration from High Resolution Multi-beam Bathymetry in Portsmouth Harbor, New Hampshire, USA (Masters Thesis). University of New Hampshire, USA.
- Fletcher, C.H., Knebel, H.J., Kraft, J.C., 1992. Holocene depocenter migration and sediment accumulation in Delaware Bay: a submerging marginal marine sedimentary basin. *Mar. Geol.* 163, 165–183.
- Goldstein, Evan B., Coco, G., Murray, A. Brad, 2013. Prediction of wave ripple characteristics using genetic programming. *Cont. Shelf Res.* 71, 1–15.
- Grant, W.D., Madsen, O.S., 1982. Movable bed roughness in unsteady oscillatory flow. *J. Geophys. Res. – Oceans Atmos.* 87, 469–481.
- Green, M.O., Vincent, C.E., Trembanis, A.C., 2004. Suspension of coarse and fine sand on a wave-dominated shoreface, with implications for the development of rippled scour depressions. *Cont. Shelf Res.* 24 (3), 317–335.
- Hay, A.E., 2008. Near-bed turbulence and relict waveformed sand ripples: observations from the inner shelf. *J. Geophys. Res. Ocean.* 113, C04040.
- Hong, L., Wan, Y.F., Jain, A., 1998. Fingerprint image enhancement: algorithm and performance evaluation. *IEEE Trans. Pattern Anal. Mach. Intell.* 20 (8), 777–789.
- Lacy, J.R., Rubin, D.M., Ikeda, H., Mokudai, K., Hanes, D.M., 2007. Bed forms created by simulated waves and currents in a large flume. *J. Geophys. Res. – Oceans* 112, C10018.
- Li, M.Z., Amos, C.L., 1998. Predicting ripple geometry and bed roughness under combined waves and currents in a continental shelf environment. *Cont. Shelf Res.* 18, 941–970.
- Madsen, O.S., Wright, L.D., Boon, J.D., Chisholm, T.A., 1993. Wind stress, bed roughness and sediment suspension on the inner shelf during an extreme storm event. *Cont. Shelf Res.* 13, 1303–1324.
- Maier, I., Hay, A.E., 2009. Occurrence and orientation of anorbital ripples in near-shore sands. *J. Geophys. Res. Earth Surf.* 114, F04022.
- Malarkey, J., Davies, A.G., 2003. A non-iterative procedure for the Wiberg and Harris (1994) oscillatory sand ripple predictor. *J. Coast. Res.* 19 (3), 738–739.
- Marsh, S.W., Vincent, C.E., Osborne, P.D., 1999. Bedforms in a laboratory flume: an evaluation of predictive models for bedform wave-length. *J. Coast. Res.* 15 (3), 624–634.
- Münchow, A., Masse, A.K., Garvine, R.W., 1992. Astronomical and nonlinear tidal currents in a coupled estuary shelf system. *Cont. Shelf Res.* 12, 471–498.
- Murray, A.B., Thieler, E.R., 2004. A new hypothesis and exploratory model for the formation of large-scale inner-shelf sediment sorting and “ripple scour depressions”. *Cont. Shelf Res.* 24, 295–315.
- Nelson, T.R., Voulgaris, G., Traykovski, P., 2013. Predicting wave-induced ripple equilibrium geometry. *J. Geophys. Res. – Oceans* 118, 3202–3220.
- Nelson, T.R., Voulgaris, G., 2014. Temporal and spatial evolution of wave-induced geometry: regular versus irregular ripples. *J. Geophys. Res. Oceans* 119, 664–668.
- Nielsen, P., 1981. Dynamics and geometry of wave-generated ripples. *J. Geophys. Res. – Oceans Atmos.* 86, 6467–6472.
- Pawlowicz, R., Beardsley, B., Lentz, S., 2002. Classical tidal harmonic analysis including error estimates in MATLAB using *t_tide*. *Comput. Geosci.* 28, 929–937.
- Pedocchi, F., García, M.H., 2009. Ripple morphology under oscillatory flow: 1. Prediction. *J. Geophys. Res.* 114, C12014.
- Raineault, N.A., Trembanis, A.C., Miller, D.C., Capone, V., 2013. Interannual changes in seafloor surficial geology at an artificial reef site on the inner continental shelf. *Cont. Shelf Res.* 58, 67–78.
- Skarke, Adam, 2013. Coastal Morphodynamics of the Estuary-Shelf Interface (PhD Dissertation). University of Delaware, USA.
- Skarke, Adam, Trembanis, A.C., 2011. Parameterization of bedform morphology and defect density with fingerprint analysis techniques. *Cont. Shelf Res.* 31 (16), 1688–1700.
- Smith, D., Sleath, J.F.A., 2005. Transient ripples in oscillatory flows. *Cont. Shelf Res.* 25, 485–501.
- Smyth, C.E., Li, M.Z., 2005. Wave-current bedform scales, orientation, and migration on Sable Island Bank. *J. Geophys. Res. – Oceans* 110, C02023.
- Soulsby, R.L., Whitehouse, R.J.S., 1997. Threshold of sediment motion in coastal environments. *Proceedings of Pacific Coasts Ports '97 Conference*, pp. 149–154.
- Soulsby, R.L., Whitehouse, R.J.S., 2005. Prediction of ripple properties in shelf seas. Mark 1 Predictor, Report TR150HR. Wallingford Ltd. UK for the ONR Ripples DRI Program.
- Soulsby, R.L., Whitehouse, R.J.S., Marten, K.V., 2012. Prediction of time evolving sand ripples in shelf seas. *Cont. Shelf Res.* 38, 47–62.
- Soulsby, R., Hamm, L., Klopman, G., Myrhaug, D., Simons, R., Thomas, G., 1993. Wave-current interaction within and outside the bottom boundary-layer. *Coast. Eng.* 21 (1–3), 41–69.
- Swart, D.H., 1974. Offshore Sediment Transport and Equilibrium Beach Profiles. Delft Hydraulics Laboratory, Delft.
- Swift, D.J.P., Moir, R., Freeland, G.L., 1980. Quaternary rivers on the New Jersey shelf: relation of seafloor to buried valleys. *Geology* 8, 276–280.
- Traykovski, P., Hay, A.E., Irish, J.D., Lynch, J.F., 1999. Geometry, migration, and evolution of wave orbital ripples at LEO-15. *J. Geophys. Res. Oceans* 104, 1505–1524.
- Traykovski, P., 2007. Observations of wave orbital scale ripples and a non-equilibrium time-dependent model. *J. Geophys. Res. – Oceans* 112, C06026.
- Trembanis, A.C., DuVal, C., Beaudoin, J., Schmidt, V., Miller, D., Mayer, L., 2013. A detailed seabed signature from hurricane sandy revealed in bedforms and scour. *Geochem. Geophys. Geosyst.* . <http://dx.doi.org/10.1002/ggge.20260> (accepted manuscript online: 23 Aug 2013)
- Trembanis, A.C., Friedrichs, C.T., Richardson, M.D., Traykovski, P., Howd, P.A., Elmore, P.A., Wever, T.F., 2007. Predicting seabed burial of cylinders by wave-induced scour: application to the sandy inner shelf off Florida and Massachusetts. *IEEE J. Ocean. Eng.* 32 (1), 167–183.
- Trembanis, A.C., Hume, T.M., 2011. Sorted bedforms on the inner shelf off north-eastern New Zealand: spatiotemporal relationships and potential paleoenvironmental implications. *Geo-Mar. Lett.* 31, 203–214.
- Voulgaris, G., and Morin, J.P., A long-term real time sea bed morphology evolution system in the south Atlantic Bight. In: *Proceedings of the IEEE/OES/CMTC Ninth Working Conference on Current Measurement Technology*, 17–19 March 2008. Charleston, SC.
- Wentworth, Chester K., 1922. A scale of grade and class terms for clastic sediments. *J. Geol.* 30 (5), 377–392.

- Wiberg, P.L., Harris, C.K., 1994. Ripple geometry in wave-dominated environments. *J. Geophys. Res. – Oceans* 99, 775–789.
- Wright, L.D., 1995. *Morphodynamics of Inner Continental Shelves*. CRC, Boca Raton.
- Wright, L.D., Xu, J.P., Madsen, O.S., 1994. Across-shelf benthic transports on the inner shelf of the Middle Atlantic Bight during the “Halloween storm” of 1991. *Mar. Geol.* 118, 61–77.
- Whitehouse, R., 1998. *Scour at Marine Structures: a Manual for Practical Applications*. Thomas Telford Publications, London (198 pp.).
- Zare, A., Cobb, J.T., 2013. Sand ripple characterization using an extended synthetic aperture sonar model and MCMC sampling methods. *IEEE Oceans – San Diego* 2013.